Supporting information for:

Capturing ring opening in photoexcited enolic acetylacetone upon hydrogen bond dissociation by ultrafast electron diffraction

Chapter 1

Quantum-chemical simulations

1.1 Trajectory surface hopping simulations

1.1.1 General information

Trajectory surface hopping molecular dynamics (TSH-MD)[1, 2] was calculated using the SHARC-MD software.[3, 4, 5] Two sets of simulations were run using the following quantum-chemical (QC) approximations:

- CASSCF(10,9)/3-21G,[6, 7, 8, 9, 10] where the QC calculations were done with OpenMolcas package,[11, 12]
- BLYP/def2-SV(P),[13, 14, 15, 16] where the QC calculations were done with Orca 5 package.[17, 18]

The active space (10,9) was chosen from calculations at the HF/3-21G level of theory, as described in section 1.1.2.

The time step in the simulations was 1 fs, the total duration of trajectories was set to 1.5 ps for the CASSCF(10,9)/3-21G dynamics and 1 ps for the BLYP/def2-SV(P) dynamics. The initial conditions were generated from the Wigner distribution for the vibrational ground state using the harmonic oscillator approximation at the same level of theory as in the simulation.

1.1.2 Results

Choosing the active space for the CASSCF

Earlier the (10,10) active space was applied in calculation [20]. Here we decided to reduce the active space to (10,9) after examining orbitals at the HF/3-21G level of theory (calculations were done with Orca 5), because the enol form of acetylacetone (AcAc) has five sp^2-hybridized atoms resulting in five π-type orbitals that need to be included in the active space, since the conjugated system (O-C-C-C-O) is being formed by five atoms of the second row of the periodic table. The frontier orbitals for AcAc are given in Fig. 1.1. During the photoexcitation and ring opening, the conjugated π-system is being broken, therefore we needed to include all of these orbitals. The lowest of the π-orbitals is the HOMO-4, therefore we need to include 10 electrons in the active space. In between the occupied π-orbitals we have two occupied σ-orbitals (HOMO-3 and HOMO-1), therefore we added two additional vacant σ-orbitals in the active space. Thus, in total nine orbitals (five occupied and four unoccupied) are used for construction of the active space.

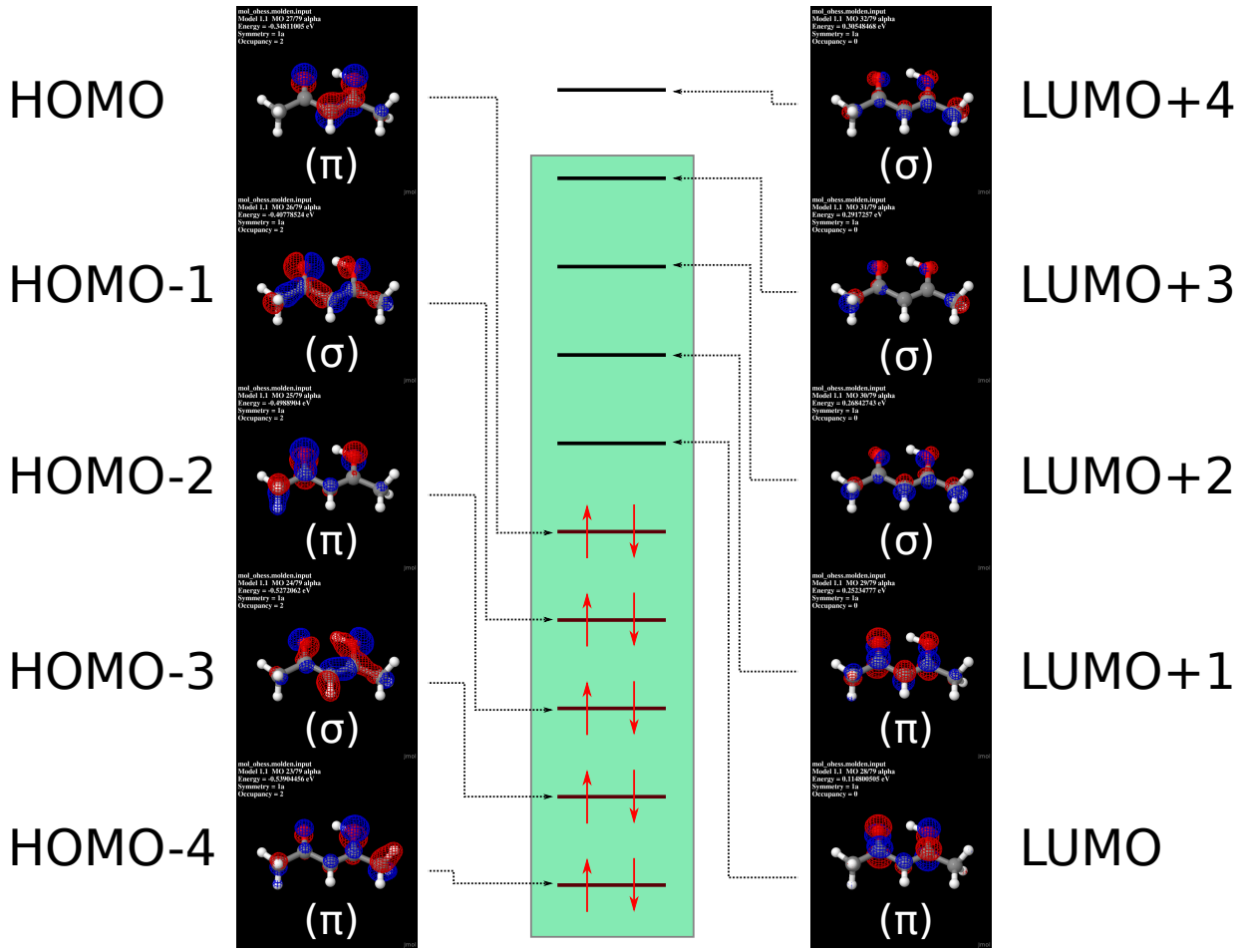

Figure 1.1: Frontier orbitals for acetylacetone at the HF/3-21G level of theory. The optimization of the structure and calculation of orbitals were done with Orca 5. Visualization was done with Jmol.[19]

Electronic states populations

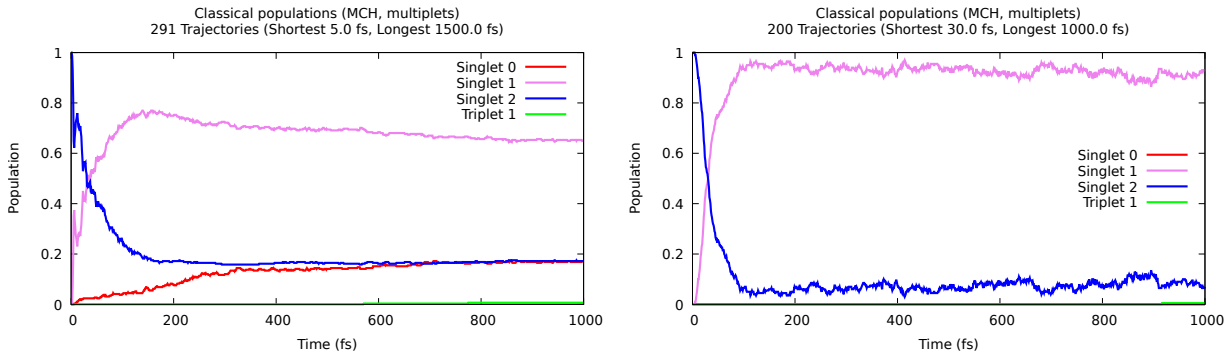

Figure 1.2: Population of the electronic states of acetylacetone in the TSH-MD simulations. Left: CASSCF(10,9)/3-21G, right: BLYP/def2-SV(P).

The two TSH-MD dynamics simulations we have performed showed very similar fast dynamics. The resulting population evolution is given in Fig. 1.2. In the DFT-based dynamics, we have not seen the $S_1 \rightarrow S_0$ relaxation in contrast to the CASSCF-based simulations. The reason might be the higher potential energy barrier needed to reach the respective conical intersection (see Fig. 1.13), which might have a different value in the TD-DFT-BLYP/def2-SV(P) calculations than in the CASSCF(10,9)/3-21G case. Both simulations showed a very small production of the T_1-state (0.7% in CASSCF and 0.5% in DFT) compared to that from Ref. [20]. This might be due to the smaller basis set in our simulations leading to a smaller spin-orbit coupling.

Internal coordinates trajectories

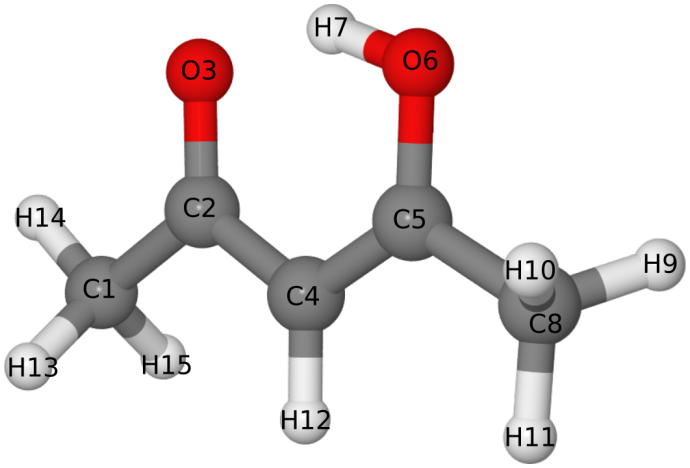

Figure 1.3: Structure and numbering of the enol form of acetylacetone with the atomic numbering.

The ring opening in AcAc can be characterized by two dihedral angles: O3C2C4C5 and O6C5C4C2 (see atom numbering in Fig. 1.3), and by the oxygen-oxygen (O...O) distance (see Fig. 1.7). In the excited S_2 state the proton transfer occurs in the $O \ldots H - O$ fragment, therefore the two unequal angles O3C2C4C5 and O6C5C4C2 will interchange. The proton transfer can be visualized by looking at the internal coordinate for the proton transfer:

$$\xi = \frac{r(\text{O3...H7}) - r(\text{O6...H7})}{2} \,, \tag{1.1}$$

where r(O3...H7) and r(O6...H7) are the distances between atoms in pairs O3–H7 and O6–H7. This is visualized in Fig. 1.8. The proton transfers readily in the S_2 state and after 200 fs becomes localized on one of the two oxygen atoms in the S_1 state when the cyclic structure is open.

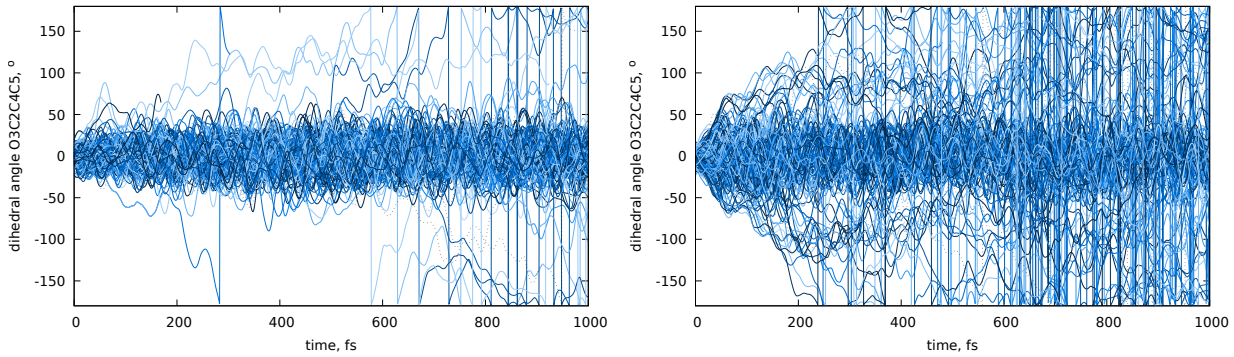

Figure 1.4: O3C2C4C5 dihedral angle variation in the TSH-MD simulations. Left: CASSCF(10,9)/3-21G, right: BLYP/def2-SV(P).

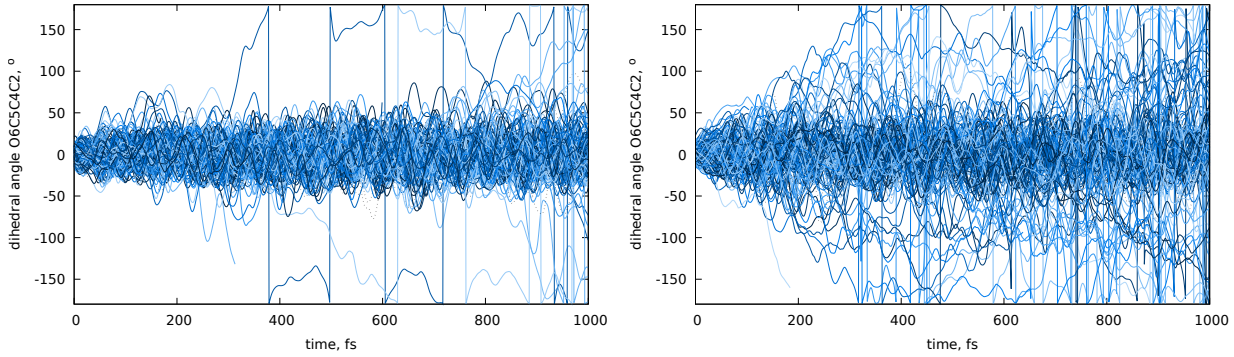

Figure 1.5: O6C5C4C2 dihedral angle variation in the TSH-MD simulations. Left: CASSCF(10,9)/3-21G, right: BLYP/def2-SV(P).

The distributions of dihedral angles O3C2C4C5 and O6C5C4C2 in the simulation are similar (Figs. 1.4 and 1.5). The ring opening thus can be visualized by looking at the OCCC dihedral distributions for both O3C2C4C5 and O6C5C4C2 angles as in Fig. 1.6.

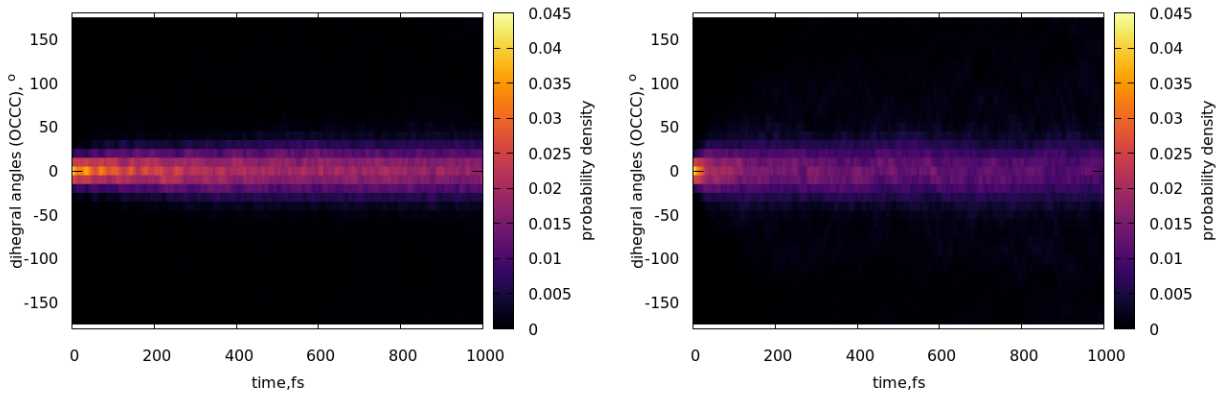

Figure 1.6: Distribution of dihedral angles for OCCC in the TSH-MD simulations. Left: CASSCF(10,9)/3-21G, right: BLYP/def2-SV(P).

Oxygen-oxygen distance increase over time is shown in Fig. 1.7. The difference in the calculated potentials at the two theory levels result in the somewhat different time behavior of the O...O distance change.

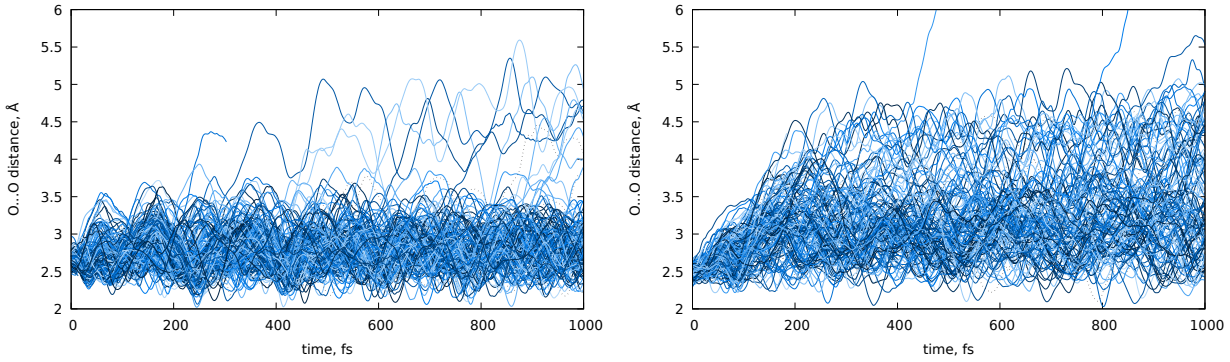

Figure 1.7: O...O distance variation in the TSH-MD simulations. Left: CASSCF(10,9)/3-21G, right: BLYP/def2-SV(P).

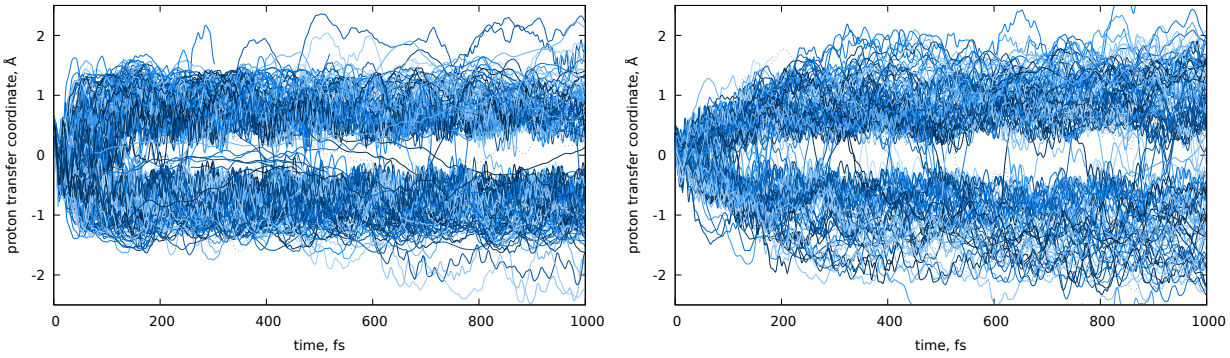

Figure 1.8: Proton transfer coordinate (Eq. 1.1) in the TSH-MD simulations representing the deviation of the proton from the position of equal distance between oxygens. Left: CASSCF(10,9)/3-21G, right: BLYP/def2-SV(P). At zero the proton is equally shared by the two atoms.

Radial distribution functions

The radial distribution functions (RDF, $f(r)$) were computed directly from the TSH-MD trajectories (see Fig. 1.9, 1.10). The $f(r,t)$ for the given times $t = 0, 50, 100, \ldots$ fs were computed. For each configuration from each trajectory

at each time step t', all the interatomic distances r_{ij} between atoms numbered $i, j = 1, 2, \ldots, 15$ $(j < i)$ contributed to the time-dependent RDF $f(r, t)$ with the weight

$$w_{ij}(t, t') = \frac{Z_i \cdot Z_j}{r_{ij}} \cdot \underbrace{\exp\left(-\frac{(t - t')^2}{\tau_{cc}^2}\right)}_{w(t,t')},$$

where $Z_i \cdot Z_j / r_{ij}$ is the approximate weight of each term for the static gas electron diffraction (GED) data[21] (Z_i and Z_j are the nuclear charges for atoms i and j), and $w(t, t')$ is the cross correlation time-dependent contribution. For the calculations, we chose the cross correlation time $\tau_{cc} = 100$ fs. The differential RDF ($\Delta f(r, t)$) was computed as $\Delta f(r, t) = f(r, t) - f(r, 0)$.

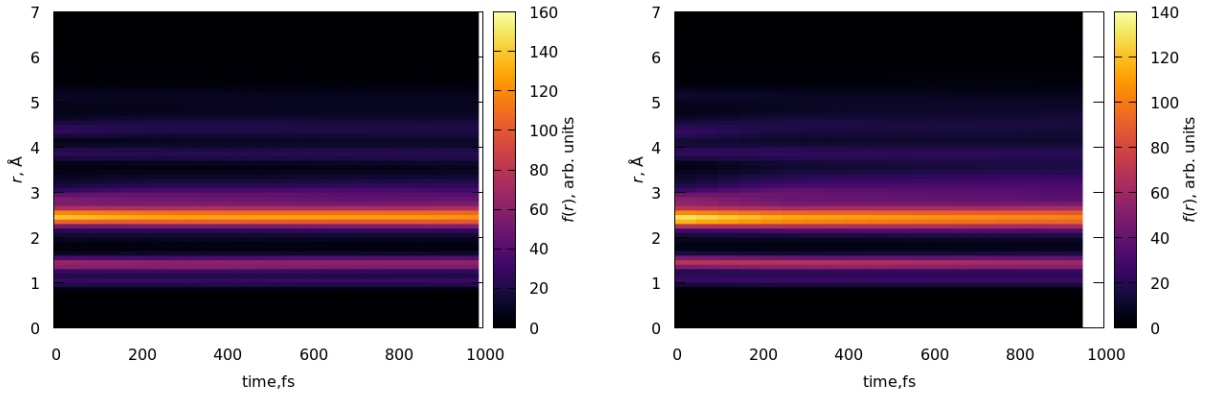

Figure 1.9: Radial distribution functions in the TSH-MD simulations. Left: CASSCF(10,9)/3-21G, right: BLYP/def2-SV(P).

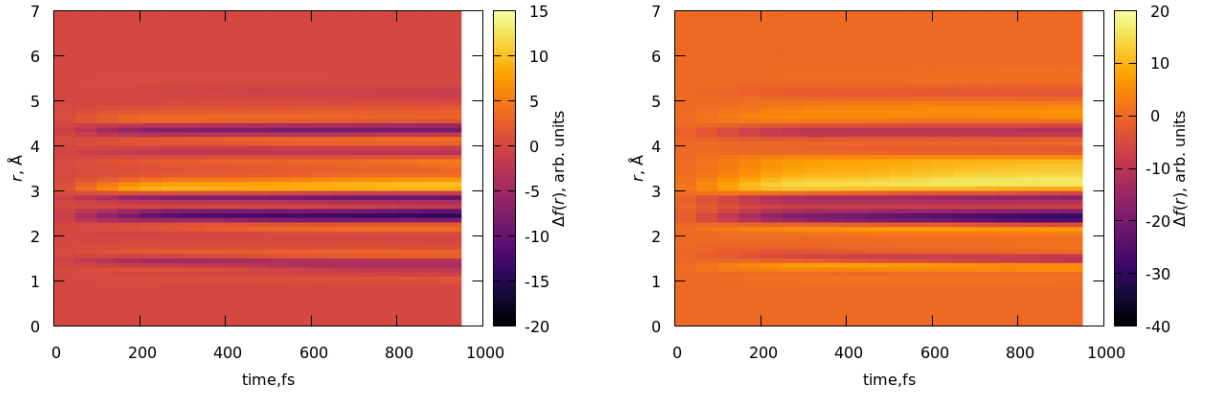

Figure 1.10: Differential radial distribution functions in the TSH-MD simulations. Left: CASSCF(10,9)/3-21G, right: BLYP/def2-SV(P).

1.2 One-dimensional cuts of the potential energy surfaces along important directions

To further understand the ring-opening dynamics in the enol-form of AcAc, we have performed one-dimensional potential energy scans along the important modes that were identified in the TSH-MD. The geometry optimizations and single point energy calculations were done at DFT (for S_0 and T_1 states) and TD-DFT (for S_1 and S_2 states) levels of CAM-B3LYP/def2-TZVP[22] theory. The calculations were performed using the Orca 5 software.[17, 18] Three modes were considered (see Fig. 1.3 for the atomic enumeration):

- two ring-opening dihedral angles, C1C2C4C5 and C2C4C5O6 (Fig. 1.11),
- and proton transfer motion (Eq. 1.1).

The geometry of AcAc was optimized for the S_0 state at different fixed values of these coordinates, giving the one-dimensional relaxed scan of the S_0 potential energy surface. The energies of the other states (S_1, S_2, and T_1) were computed at the given frozen optimized geometries. The results are given in Figs. 1.11 and 1.12. In addition to that, we have performed a relaxed potential scan along the ring-opening dihedral angles (C1C2C4C5 and C2C4C5O6). These scans revealed a direct pathway for the $S_1 \rightarrow S_0$ relaxation via a conical intersection.

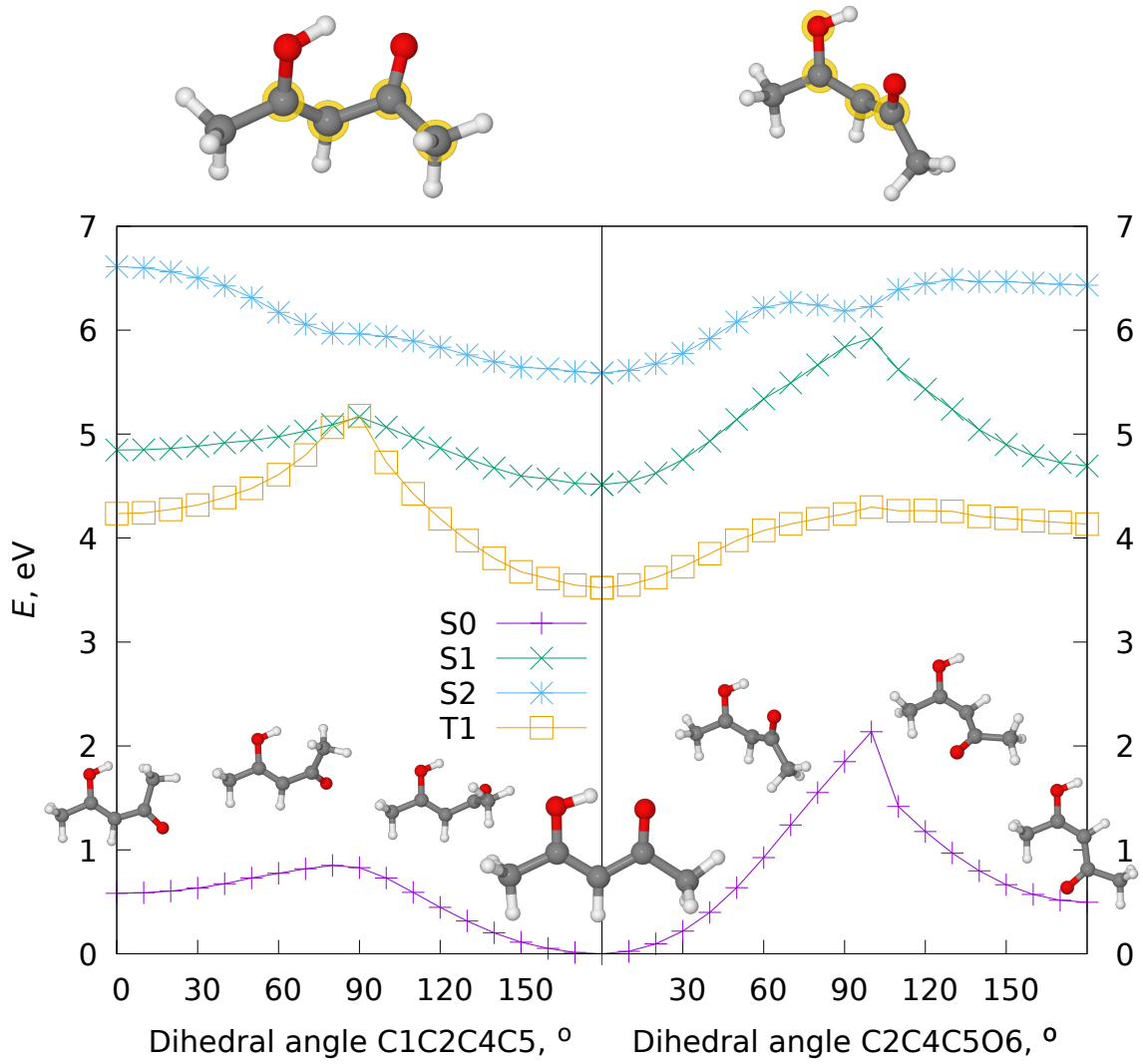

Figure 1.11: Potential energy scans of the ring-opening dihedral angles. The optimization of the geometries along these coordinates were done at the S_0 state, and the energies of the other states (S_1, S_2, T_1) were computed at the S_0-optimized geometries. The upper geometries show the scanned dihedrals (defining atoms are given in yellow at the top of the figure), the structures in the plot show the intermediate geometries of the scan. The atomic enumeration is given in Fig. 1.3.

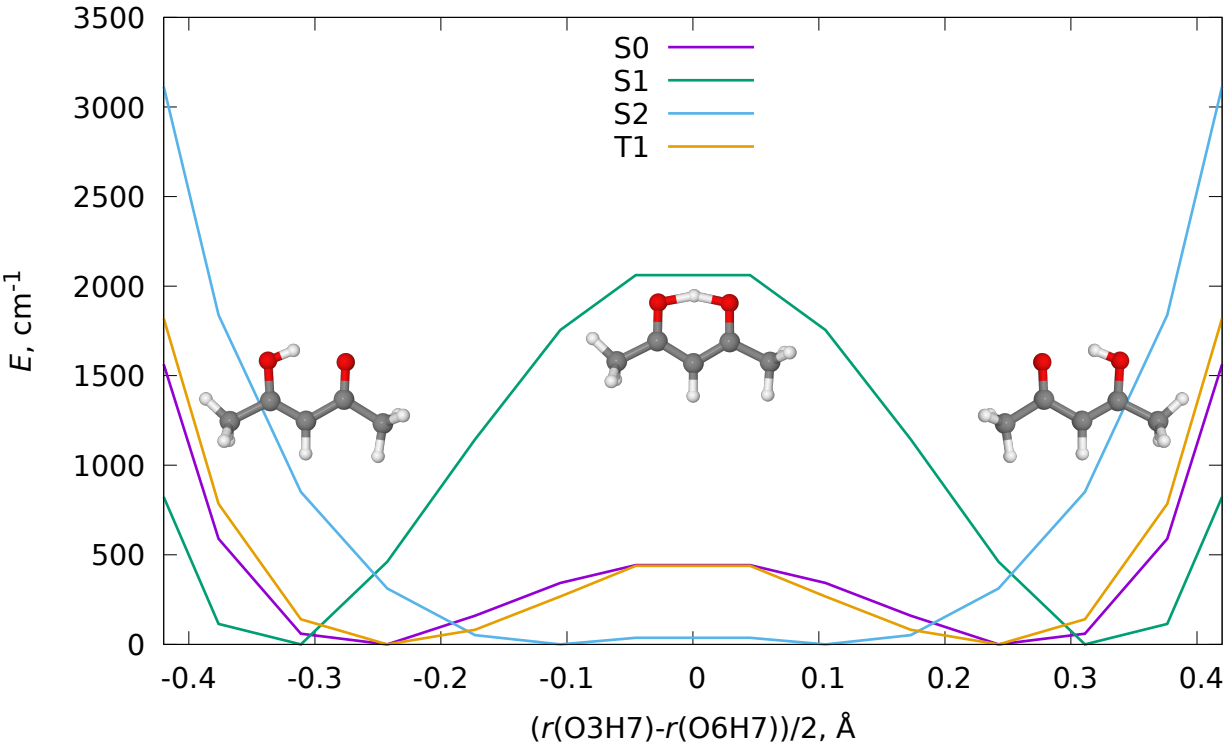

Figure 1.12: Potential energy scans of the proton transfer coordinate. The optimization of the geometries along this coordinate were done at the S_0 state, the energies of the other states (S_1, S_2, T_1) were computed at the S_0-optimized geometries. The structures in the plot show the geometries of AcAc near the equilibrium and the transition states. The atomic enumeration is given in Fig. 1.3.

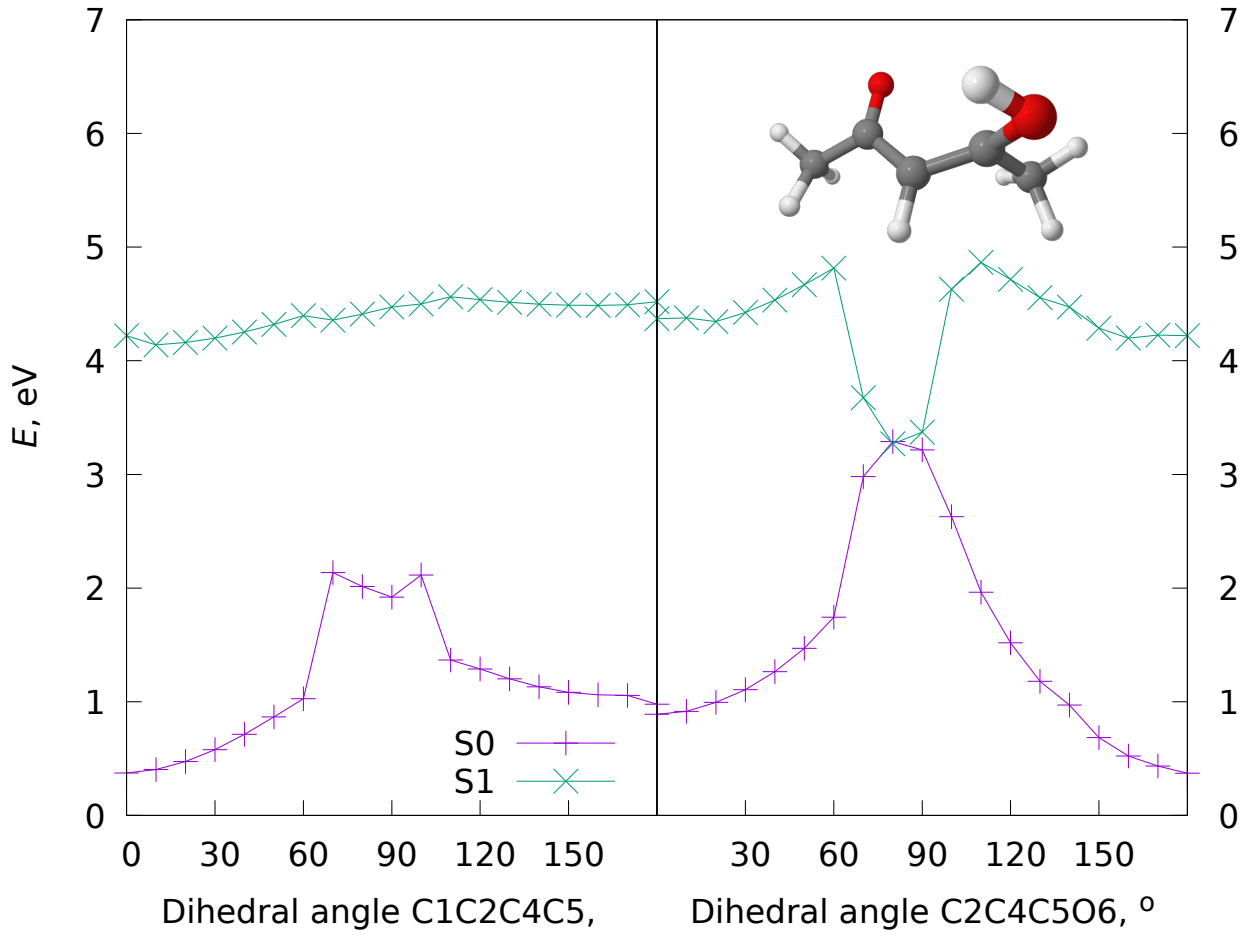

Figure 1.13: Potential energy scans of the ring-opening dihedral angles. The optimization of the geometries along these coordinates were done at the S_1 state, the energies of the other states (S_0, S_2, T_1) were computed at the S_1-optimized geometries. The scans are an approximation to the $S_1 \rightarrow S_0$ conical intersection. The atomic enumeration is given in Fig. 1.3.

Chapter 2

Analysis of the gas electron diffraction data

2.1 Scattering factors

Special attention is required for calculating the scattering factors of MeV-electrons. Here we used UNEX software [23] for this purpose. Until now the allowed range of electron energies in UNEX for processing the gas electron diffraction data was limited to 10–90 kV. In the course of this work we implemented several new methods for calculating the scattering factors of MeV-electrons based on available data in literature. In the present work we used the most accurate and affordable method as a combination of elastic and inelastic scattering factors, see Eq. 4.3.3.2 in [24]. For the amplitudes of the elastic scattering the data from the first Born approximation given in Table 4.3.2.3 of [24] was utilized. The computed amplitudes were further corrected for relativistic effects and a term due to the squared atomic Coulomb potential was added as suggested (see Eq. 13 in [25]) earlier. The inelastic scattering factors, required for the calculation of the purely atomic part of the total scattering, were computed from the published data obtained in Morse approximation (see Table 4.3.3.2 in [24]). In this work we could not use the partial wave elastic scattering factors, since they were not available for MeV-electrons. Thus, the phases η in Eq. 4.3.3.2 in [24] were assumed to be equal, which then cancel out and do not lead to phase-shift effect. This is a fairly accurate approximation for combinations of atoms without large differences in nuclear charge Z, which is applicable to AcAc molecule.

2.2 Extraction of the data

We applied a multi-step procedure of data analysis to extract the scattering and structural information about the intermediate structures.

2.2.1 Static analysis of the AcAc

First, we performed the analysis of the static structures of the AcAc molecule. The general scattering intensity in gas electron diffraction (GED) is given as

$$I(s) = I_{\mathrm{m}}(s) + \underbrace{I_{\mathrm{at}}(s) + I_{\mathrm{n}}(s)}_{I_{\mathrm{b}}(s)} \ .$$

Here, $s = \frac{4\pi}{\lambda}\sin(\theta/2)$ is the scattering coordinate related to the electrons wavelength λ and scattering angle θ, showing the deviation of the direction of the scattered electrons from the original direction. The intensity consists of three contributions: I_{m} – molecular scattering, showing the interference of the scattering waves from the different atoms, I_{at} – atomic scattering on the individual atoms, and I_{n} – systematic and random noise. The latter two contributions we can combine into a single background contribution I_{b}. Instead of the absolute molecular intensity, it is more convenient to use the reduced molecular scattering function

$$sM(s) = s \cdot \frac{I_{\mathrm{m}}(s)}{I_{\mathrm{b}}(s)} = s \cdot \left(\frac{I(s)}{I_{\mathrm{b}}(s)} - 1 \right) \ , \tag{2.1}$$

which can be also written as[21]

$$sM(s) = \sum_i \sum_{j<i} g_{ij}(s) \cdot \left\langle \frac{\sin(sr_{ij})}{r_{ij}} \right\rangle \ , \tag{2.2}$$

where g_{ij} are the scattering factor of the atomic pair formed by atoms numbered i and j, sums are iterating over all the atoms in the molecule, r_{ij} is the interatomic distance between atoms i and j, s is the scattering coordinate, and

$\langle \ldots \rangle$ is the thermal averaging of the r_{ij}. Usually, this scattering function is transformed into the function $f(r)$ through the sine-Fourier transform, as

$$f(r) = \int_0^{+\infty} sM(s) \cdot \sin(sr) \cdot \exp(-a \cdot s^2) ds \ ,$$

where a is the damping factor to mitigate the usual shortness of the GED experimental data due to fast (s^{-4}) decay of the atomic scattering. $f(r)$ is related to the pair distribution function (PDF) as $f(r) = \mathrm{PDF}(r) \cdot r$. To account for uncertainties of the $sM(s)$ points, the sine-Fourier transform was done using the regularized weighted sine least-squares spectral analysis (rwsLSSA) approach.[26]

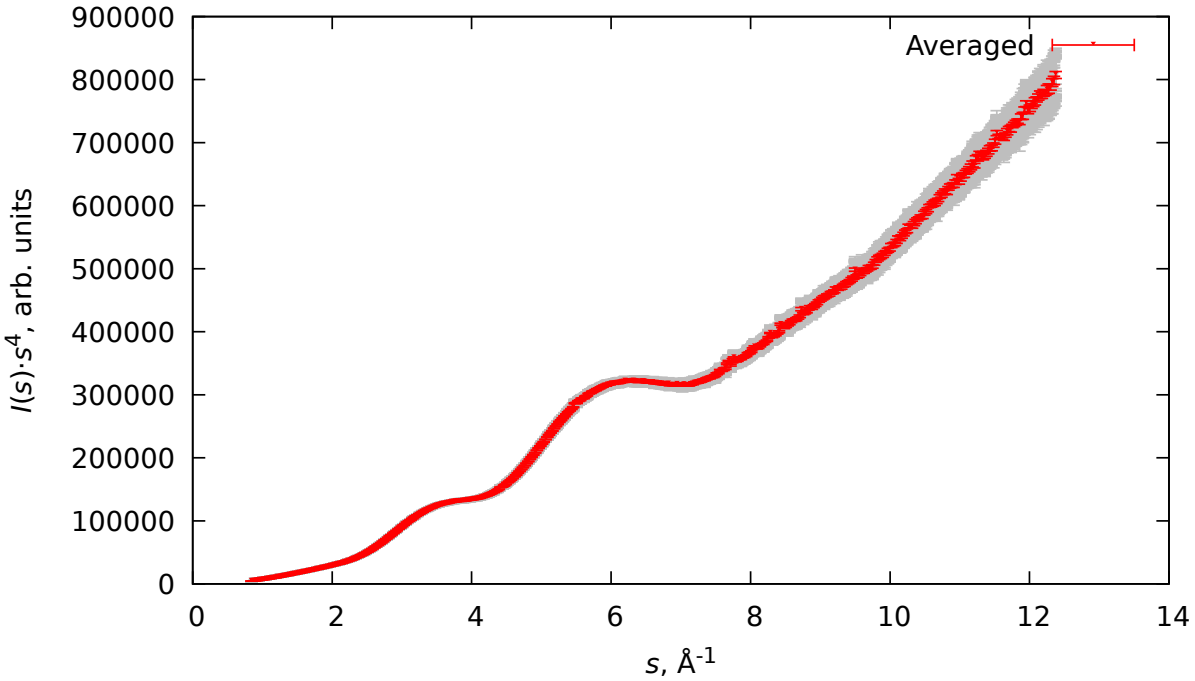

Figure 2.1: Individual scattering intensities of acetylacetone in static regime (for the pump-probe delays, when electron pulse arrives before the laser pulse, i.e., $t < t_0$), in gray. The red curve and points represent the averaged data. To compensate for the decay of the atomic scattering, the intensities were multiplied by s^4.

We assume, that the background is approximately the same during the whole duration of the pump-probe experiment. Therefore, we can extract the background for the static system (for the pump-probe delays, when electron pulse arrives before the laser pulse, i.e., $t < t_0$), and then apply the same background to the whole range of pump-probe delays. The intensities of the seventeen individual intensities for delays t in range from -3.00 ps to -0.15 ps were averaged as

$$I_{\mathrm{av}}(s) = \frac{\sum_{k=1}^{17} w_k I_k(s)}{\sum_{k=1}^{17} w_k} \ , \tag{2.3}$$

where k iterates through the chosen delays of the data, I_k is the data for the k-th pump-probe delays t_k, and $w_k = 1/\sigma_k^2(s)$ is the weight of the data point calculated from the standard deviation σ of the individual point. The standard deviations of each averaged data point were then calculated as

$$\sigma_{\mathrm{av}}^2(s) = \frac{1}{17} \sum_{k=1}^{17} (I_k(s) - I_{\mathrm{av}}(s))^2 \ .$$

The results are given in Figure 2.1.

The resulting averaged intensity for the static structure of AcAc was fitted using the regularization of the internal coordinates.[27, 28] At the temperatures of the experiment ($T = 323$ K), AcAc exists nearly completely in the enol-form.[29] The parameters used for the regularization were obtained from the quantum-chemical calculations at PBE0-D3BJ/def2-QZVPP level of theory.[30, 31, 16] The vibrational amplitudes and the anharmonic corrections to the averaged distances were computed using the VibModule software[32] from the harmonic and cubic anharmonic force fields of AcAc obtained at the B3LYP-D3BJ/def2-TZVPP level of theory.[13, 14, 33, 31, 16] The quality of the analysis was judged using the weighted R-factor given by

$$wR_f = \sqrt{\frac{\sum_i w_i \left(sM^{(\mathrm{exp})}(s_i) - sM^{(\mathrm{model})}(s_i)\right)^2}{\sum_i w_i \left(sM^{(\mathrm{exp})}(s_i)\right)^2}} \times 100\% \ ,$$

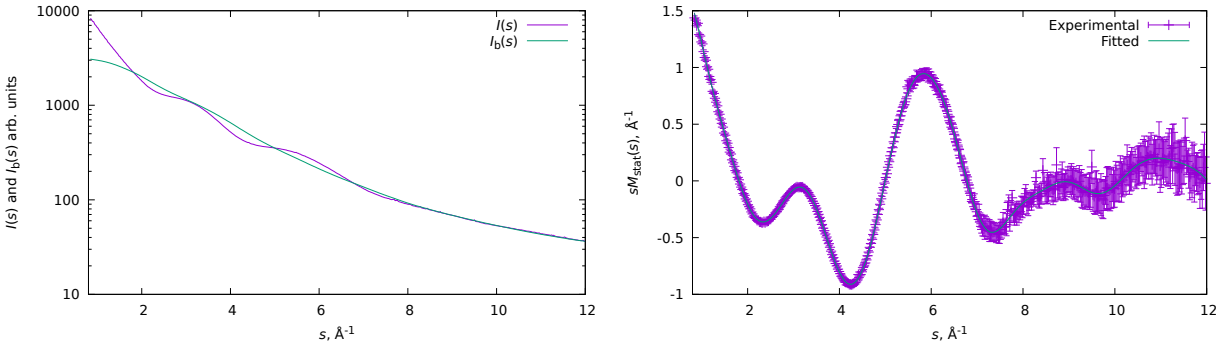

Figure 2.2: Left: intensity and background curves for the static GED data of AcAc. Right: comparison of the experimental (points) and fitted $sM(s)$ for the AcAc, the error bars represent $\pm 3\sigma$ window.

where "exp" denotes the experimental data, "model" denotes the fitted model, and the $w = 1/\sigma^2$ are the weights of the individual data points. The resulting wR_f was found to be 2 %. The intensity, background, and the comparison of the $sM(s)$ is given in Fig. 2.2.

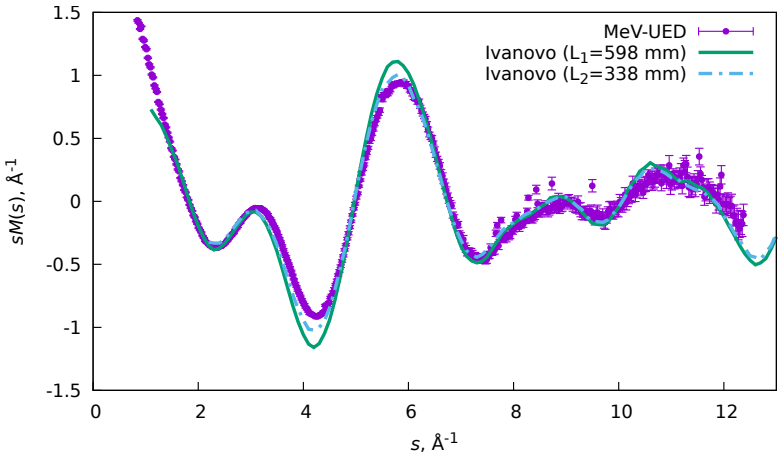

Figure 2.3: Comparison of the experimental $sM(s)$ curves of AcAc obtained using the MeV-UED setup (this work) and combined GED+MD apparatus at the Ivanovo State University of Chemistry and Technology (ISUCT). The data from Ref. [29] are the courtesy of Profs. N.V. Belova and G.V. Girichev. The two L denote two measured nozzle-to-screen distances.

The obtained experimental $sM(s)$ were compared with the previous structural investigation of the AcAc molecule done at the Ivanovo State University of Chemistry and Technology (ISUCT). This structural GED study was carried out with a combined GED+MS apparatus and published in Ref. [29]. The comparison shows general agreement between the two sets of data. The difference in the spectral frequencies comes from the different electron wavelengths in the experiments, which results in different atom-atom scattering profiles. However, the general compatibility of the oscillation frequencies indicated a correct determination of wavelength in the current experiment.

2.2.2 Extraction of the real-space dynamical evolution of the system

The rwsLSSA procedure, unfortunately, cannot provide a high enough resolution of the real-space dynamics to extract the dynamical behavior of the system. Therefore, an alternative approach was applied. The simplistic time-dependent differential reduced molecular scattering functions $\Delta sM_{\mathrm{simple}}(s,t)$ were calculated as

$$\Delta sM_{\mathrm{simple}}(s,t) = \frac{I_t(s) - I_{\mathrm{av}}(s)}{I_{\mathrm{at}}(s)} \ , \tag{2.4}$$

where $I_{\mathrm{av}}(s)$ is the static ensemble scattering intensity, given with Equation 2.3, $I_t(s)$ is the pump-probe delay (t)-dependent scattering intensity, and the $I_{\mathrm{at}}(s)$ is the corresponding atomic scattering intensity, computed using the UNEX software. The resulting map in the least noisy region of small $s < 7$ Å^{-1}, is given in Figure 2.4. The map unambiguously shows a dynamic change in the system. To trace these dynamics with the change in the interatomic distances, we performed a weighted least-squares (wLSQ) fitting of the $\Delta sM_{\mathrm{simple}}(s,t)$ dependencies for the $t \geq 100$

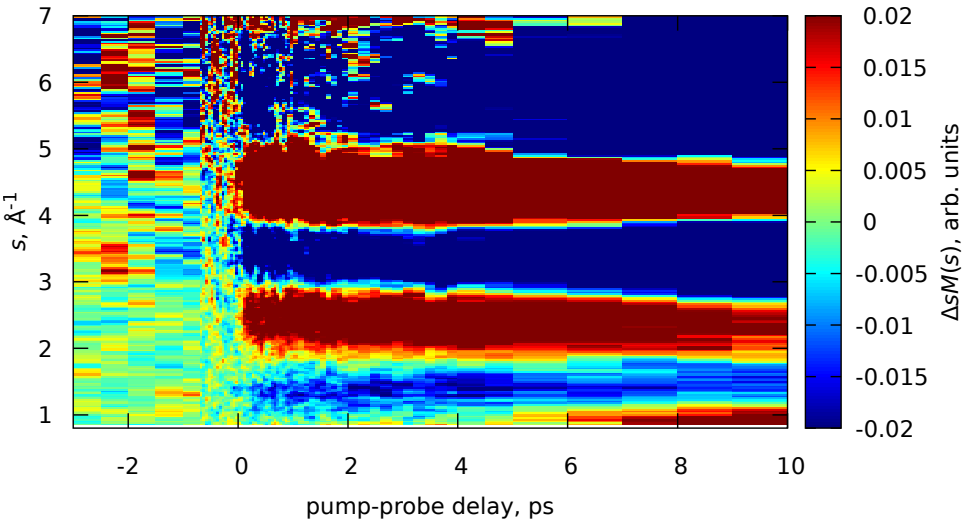

Figure 2.4: The pump-probe dependent difference map of the reduced molecular scattering (Equation 2.4). The color of the points shows the relative contribution value a_k.

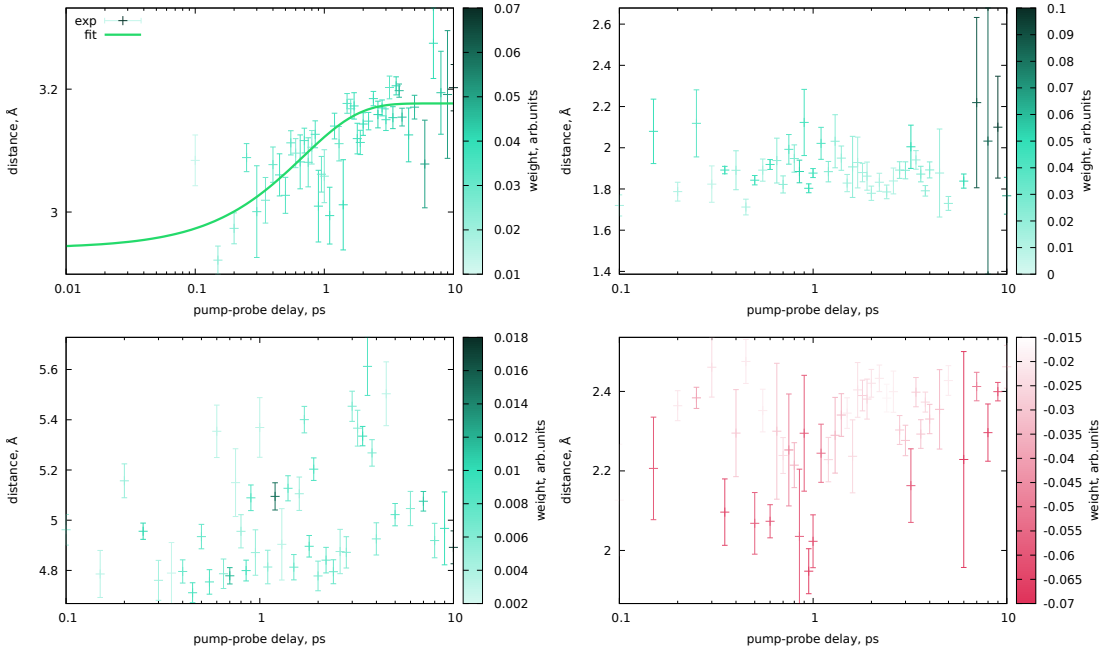

Figure 2.5: Fitted contributions of the intermolecular distances changes according to Equation 2.5. The four panels represent the components of the diffraction signal.

fs (with sufficient signal-to-noise ratio) with an equation

$$\Delta sM_{\text{model}}(s,t) = \sum_{k=1}^{4} a_k \cdot \exp\left(-\frac{s^2 l_k^2}{2}\right) \cdot \sin(s \cdot r_k) \ , \tag{2.5}$$

where a_k are the relative contributions of the different pair distance dynamics, l_k are the vibrational amplitudes and r_k are the interatomic distances. Since we fit the differential curves, we expect some of the weights a_k to be positive (newly formed distances), and some – negative (depletion of the initial unexcited ensemble). A satisfactory fit for each pump-probe delay was found to be achievable with four contributions. Three of the weights were positive, and one negative. The results are given in Figure 2.5. The newly formed distances are grouped around 3 Å, 2 Å, and 5 Å, while depleted terms are approximately at 2.4 Å. The latter corresponds to the most intense non-covalently bonded distance peak in the static radial distribution functions. The first peak shows clear exponential dynamics, therefore the time-dependence $r_k(t)$ was fitted with a function $r_\infty - \delta r \cdot \exp(-t/\tau)$, where r_∞ is the final value of this distance term at the infinite pump-probe delay t, δr is the change in magnitude, and τ is the relaxation time. The results of the wLSQ fit are: $r_\infty = 3.177 \pm 0.008$ Å, $\delta r = 0.24 \pm 0.3$ Å, and $\tau = 0.7 \pm 0.2$ ps. This can be attributed to the

expansion of the molecule due to the ring opening.

2.2.3 Extraction of the time-dependent excited ensemble scattering profiles

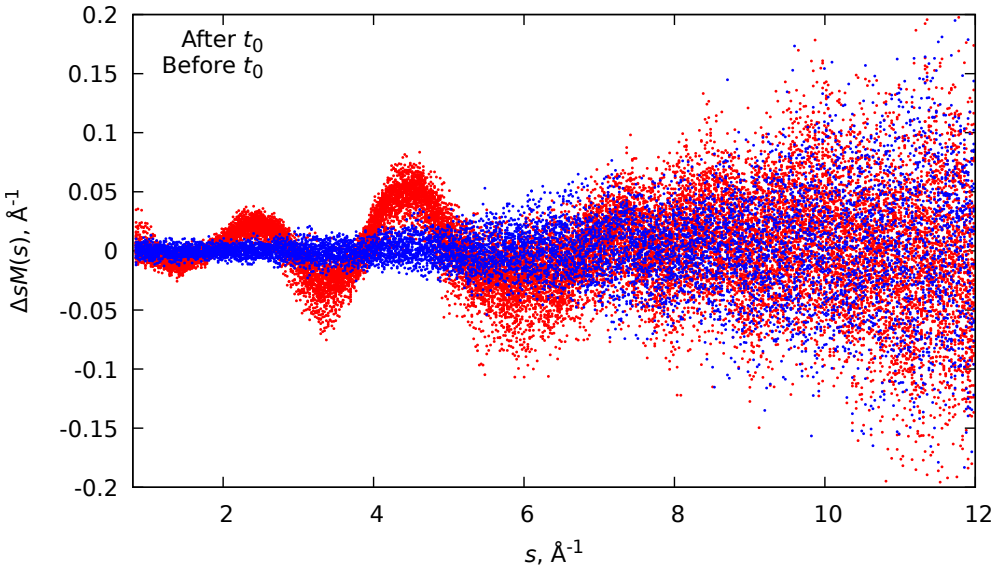

Figure 2.6: Comparison of the differential reduced molecular scattering functions $\Delta sM(s)$ (Equation 2.6) for the pump-probe delays before t_0 (blue dots) and after t_0 (red dots). All the $\Delta sM(s)$ are illustrated in the same figure.

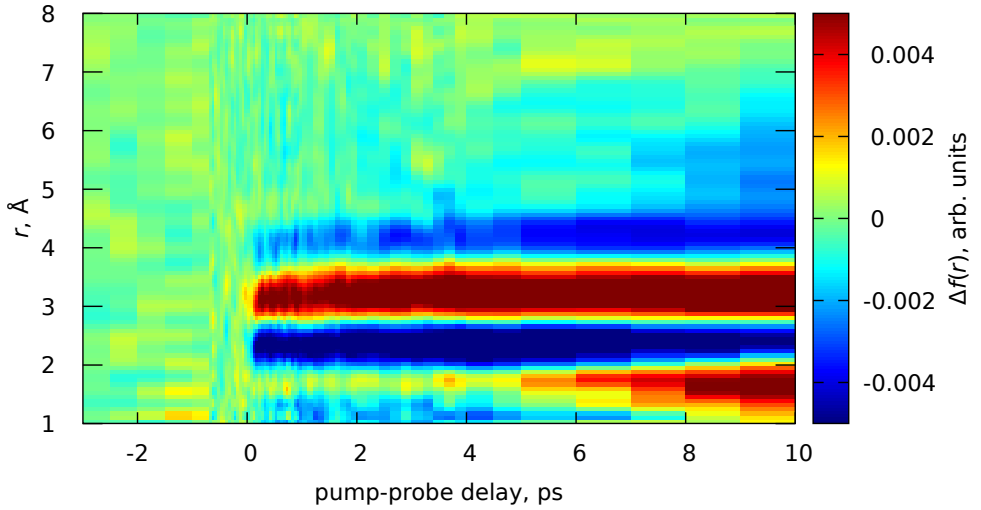

Figure 2.7: Differential radial distribution functions (RDF) $\Delta f_t(r)$. The RDF was obtained by the regularized weighted least-squares spectral analysis (rwLSSA)[26] of the experimental difference $sM(s)$ functions (Figure 2.4), divided by the g-factor for the oxygen-oxygen term, and multiplied by a damping function $\exp(-a \cdot s^2)$ with a damping factor $a = 0.05$ Å^2, the regularization parameter $\alpha = 10^5$.

After obtaining the background of the GED from the static GED data for the AcAc ($I_{\mathrm{b}}^{(\mathrm{stat})}$), we analyzed the delay-dependent data. For each pump-probe delay t, we have the correspondent GED intensity $I_t(s)$. The time-dependent reduced molecular intensity was then computed as in Equation 2.1:

$$sM_t(s) = s \cdot \left(\frac{I_t(s)}{I_{\mathrm{b}}^{(\mathrm{stat})}} - 1 \right) .$$

To see the presence of the pump-probe dynamics, we have plotted the differential $sM(s)$, defined as

$$\Delta sM_t(s) = sM_t(s) - sM_{\mathrm{stat}}(s) , \tag{2.6}$$

where $sM_{\text{stat}}(s)$ is the experimental static $sM(s)$ obtained for the structural analysis of AcAc for $t < t_0$. The results are given in Figure 2.6. As one can see, after the t_0, there is a clearly visible change of the $sM_t(s)$. When performing the wLSSA on the $\Delta sM_t(s)$ obtaining $\Delta f_t(r)$ (Fig. 2.7), we see the changes in the intermolecular distances.

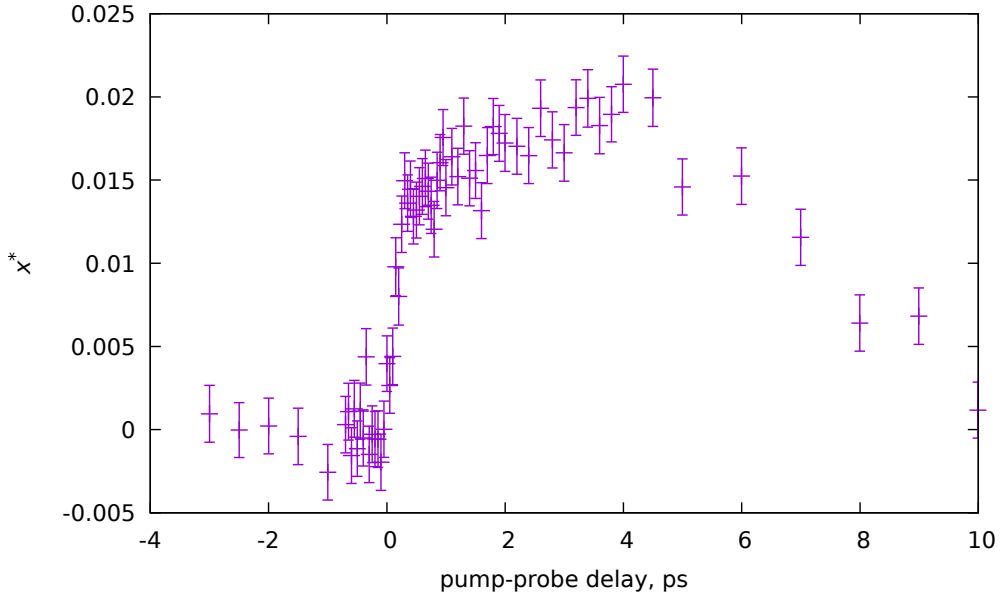

Figure 2.8: Relative amount of the excited molecules x* in the scattering data (see definition of x* in Equation 2.7).

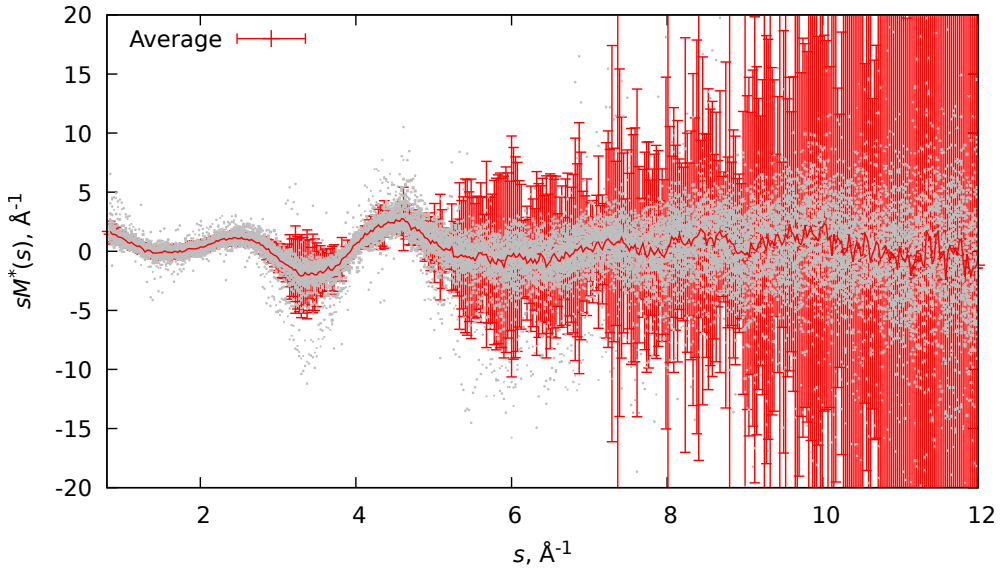

Figure 2.9: Intermediate's reduced molecular scattering functions $sM_t^*(s)$ computed with Eq. 2.8, and their average values over all pump-probe delays. Gray points represent individual measurements for pump-probe delays after t_0.

To further analyze the GED patterns, we extract the scattering patterns of the ensemble of the excited structures ($sM_t^*(s)$), that we will denote further as "intermediate". The $sM_t(s)$ at each pump-probe delay can be represented as

$$sM_t(s) = \underbrace{x}^{(1-x^*)} \cdot sM_{\text{stat}}(s) + \overbrace{(1-x)}^{x^*} \cdot sM_t^*(s) \ , \tag{2.7}$$

where $sM_{\text{stat}}(s)$ is the background signal of the molecules, that did not absorb the UV photons, staying in the same initial state, the $sM_t^*(s)$ is the scattering signal of the excited ensemble, and x^* and x are the relative amounts of the excited and unexcited molecules ($x + x^* = 1$). From the comparison of the total $sM_{\text{stat}}(s)$ curve (Fig. 2.2) with the $\Delta sM_t(s)$, we see that the differential signal is an order of magnitude smaller than the total signal, therefore the x^* is expected to be small. We estimate the x from the linear least-square fitting of the $sM_{\text{stat}}(s)$ signal to the $sM_t(s)$, as

$$\Phi(x) = \sum_i w_i (sM_t(s_i) - x \cdot sM_{\text{stat}}(s_i))^2 \to \min \ \Rightarrow \frac{d\Phi(x)}{dx} = 0 \ ,$$

where weights are $w_i = 1/(\sigma_i^{\text{stat}} \cdot \sigma_i(t))$. The solution is given as

$$x = \underbrace{\left(\frac{\sum_i w_i \left(sM_t(s_i) \cdot sM_{\text{stat}}(s_i) \right)}{\sum_i w_i \left(sM_{\text{stat}}(s_i) \right)^2} \right)}_{\overline{x}} \pm \underbrace{\left(\frac{1}{\sum_i w_i \left(sM_{\text{stat}}(s_i) \right)^2} \right)}_{\sigma_x} .$$

The resulting x^* can be computed as $x^* = (1 - \overline{x}) \pm \sigma_x$. Such dependencies are plotted in Figure 2.8. For the cases, when there is enough certainty of the presence of the new species in the GED data (i.e. when $|x - 1| \geq \sigma_x$), the intermediate $sM_t^*(s)$ can be extracted as

$$sM_t^*(s) = \frac{sM_t(s) - \overline{x} \cdot sM_{\text{stat}}(s)}{1 - \overline{x}} . \tag{2.8}$$

If we plot these dependencies (Figure 2.9), we see that in general the shape of the scattering functions looks similar for $s < 6$ Å^{-1}. Therefore, we have averaged the signal of the intermediate's ensemble for all the pump-probe delays $t > t_0$, and performed a structural analysis of this mixture of new species.

2.3 Structural analysis of the intermediate ensemble

2.3.1 Structure fitting model

To perform the structural analysis, we utilized the standard static GED model. The following simplifications were further applied.

- The real excited state ensemble, according to the TSH-MD simulations (see section 1), shows a large variety of structures. However, construction of the multi-conformer or dynamic models without theoretical background is a complicated task. Therefore, the least-squares refinement of the structure was done in a simplified static model of GED, where the scattering data are being represented by a single structure,[34] where the vibrationally-averaged structure (Eq. 2.2) is given by the expression:[21, 35, 36]

$$\left\langle \frac{\sin(sr)}{r} \right\rangle \approx \exp\left(-\frac{l^2 s^2}{2} \right) \cdot \frac{\sin(sr_a)}{r_a} ,$$

  where $l^2 = \langle r^2 \rangle - \langle r \rangle^2$ is the vibrational amplitude and $r_a = \langle r^{-1} \rangle^{-1} \approx \underbrace{\langle r \rangle}_{r_g} - \frac{l^2}{r_e}$ (r_e denotes the equilibrium distance).

- The geometrically inconsistent r_a-structure requires computation of the $r_a - r_e$ corrections, however for the excited state ensemble this is impossible to do directly because of the unknown accuracy of the applied quantum-chemical approximations, as well as of the unknown representation of the ensemble from the TSH-MD, and due to the absence of the nuclear quantum effects.[35, 36, 37] Therefore, the effective structure was represented in a geometrically consistent fashion by a three-dimensional molecular structure, where the effective interatomic distances are having the meaning of the r_a distances.

- The interatomic amplitudes l also cannot be determined from the MD simulations, since they require the localization of the structure.[36] Therefore the amplitudes of the interatomic distances between atoms numbered i and j were represented as

$$l^2 = l_i^2 - \alpha l_i l_j + l_j^2 ,$$

  where l_i and l_j are the amplitudes of a single atom, and the $\alpha \in [0; 2]$ is the correlation parameter with $\alpha = 0$ being no correlation between the atomic vibrations, and $\alpha = 2$ is the correlated motions of the atoms. For the unbonded distances the α was set to zero, while for the bonded distances it was found set to $\alpha = 1$, a value determined from the numeric tests on the static GED data of AcAc.

The GED model of the AcAc molecule was given by a Z-matrix, where all the bonds with hydrogen atoms were set to 1.0 Å, the valence angles XYH (X,Y=C,O) were set to 120°, and the dihedral angles were set to keep the tetrahedral configurations of the methyls and the planar configuration of CC(= O)C and of the hydrogen-containing fragments. The other geometrical parameters (bonds, valence angles between the second period atoms, and the backbone two internal rotation angles) were allowed to float. The bonds were constrained to be in the range between 1.2 and 1.9 Å, the valence angles – from 100° to 140°, and the two internal rotation dihedrals did not have any restrictions. The atomic amplitudes were allowed to float between 0.005 Å and 1.5 Å. The GED scattering curves were obtained using the UNEX software[23], and the total optimization was done in a home-written Python script using the Differential Evolution algorithm[38] as implemented in SciPy[39] library.

Due to the inverse problem in GED being ill-posed and the existence of many equivalent local minima,[40] we do not perform the estimation of the parameters uncertainties or claim the obtained structures to be a representative

combination of the best fitting structures. The main purpose of this type of structural analysis is to visualize the main changes in the AcAc structure occurring after the UV excitation. Due to the stochastic nature of the differential evolution algorithm and due to the multiple possible local least-squares functional minima, we perform the structure search at least five times per GED $sM(s)$ curve.

2.3.2 Test on the static GED data

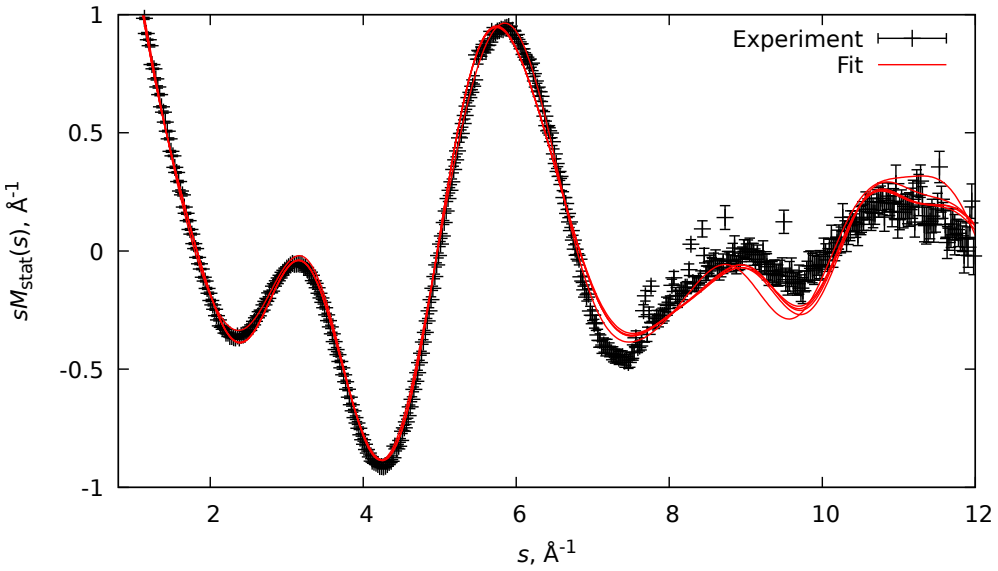

Figure 2.10: Comparison of the experimental and fitted $sM_{\mathrm{stat}}(s)$ in case of the crude molecular fitting model. Different fit curves show the results of five independent fits.

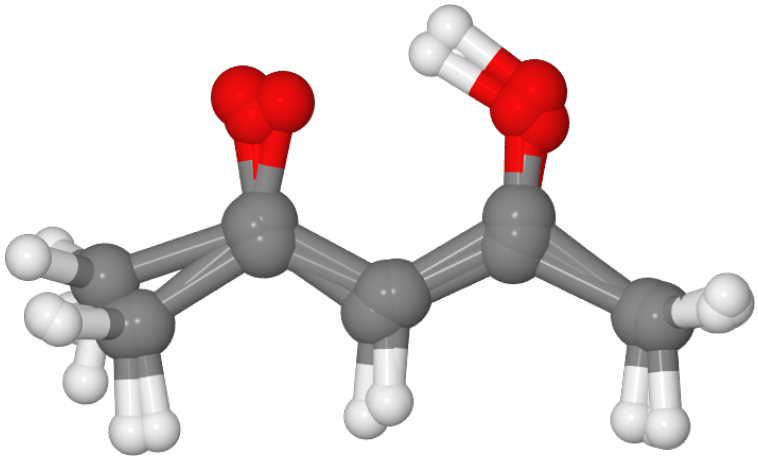

Figure 2.11: Comparison of the five AcAc structures refined from the analysis of static scattering curves ($sM_{\mathrm{stat}}(s)$).

To test the performance of the procedure, it was applied to the static GED data of AcAc (for $t < t_0$). Five optimizations with the differential evolution algorithm were performed, obtaining the unique planar conformer of AcAc (Fig. 2.11). The wR_f for the obtained structures were in the range from 5.3 % to 5.6 % (see Fig. 2.10). Due to the lower quality of the model, the obtained results are almost three times greater than the refined value with the classical GED analysis (2.0 %).

2.3.3 Fitting of the intermediate structure

For the averaged intermediate scattering $sM^*(s)$ curve we performed 25 optimizations of structures. The resulting wR_f were in range from 20.9 % to 27.5 % (Fig. 2.12). The agreement is worse because we try to describe multi-pump-probe delay data with multiple conformers in a single-structure model. The final 26 structures were clustered by their structural similarity using the `findUniqueConformers` script of the MOLINC repository.[41] The script has found four types of structures, which are given in Fig. 2.13. As one can see, all of the structures show open-cycle structure, which agrees with the simulations. The structures also show a large increase in the bond lengths

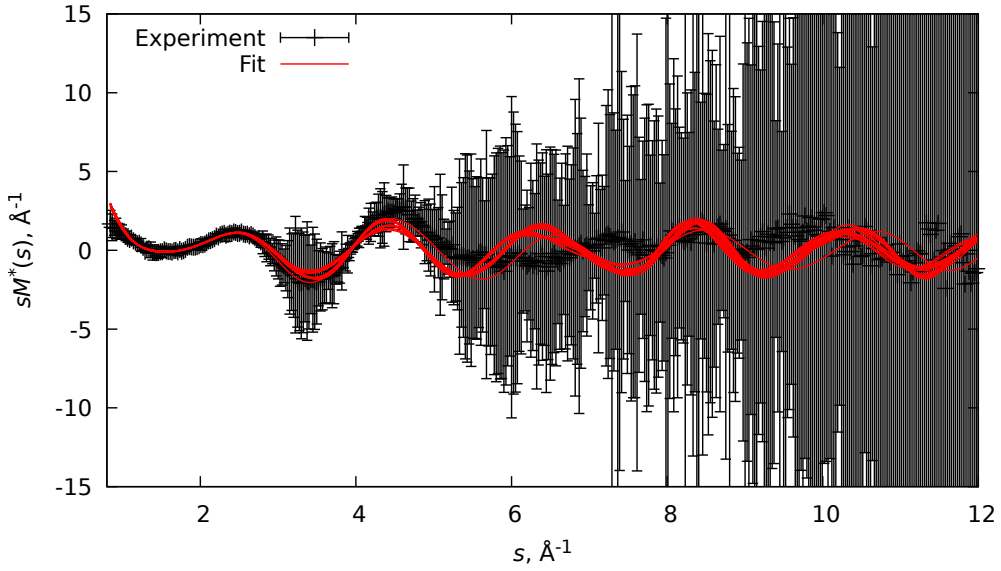

Figure 2.12: Comparison of the experimental and fitted $sM_{\mathrm{stat}}(s)$ in case of the crude molecular fitting model. Different fit curves show the results of 25 independent fits.

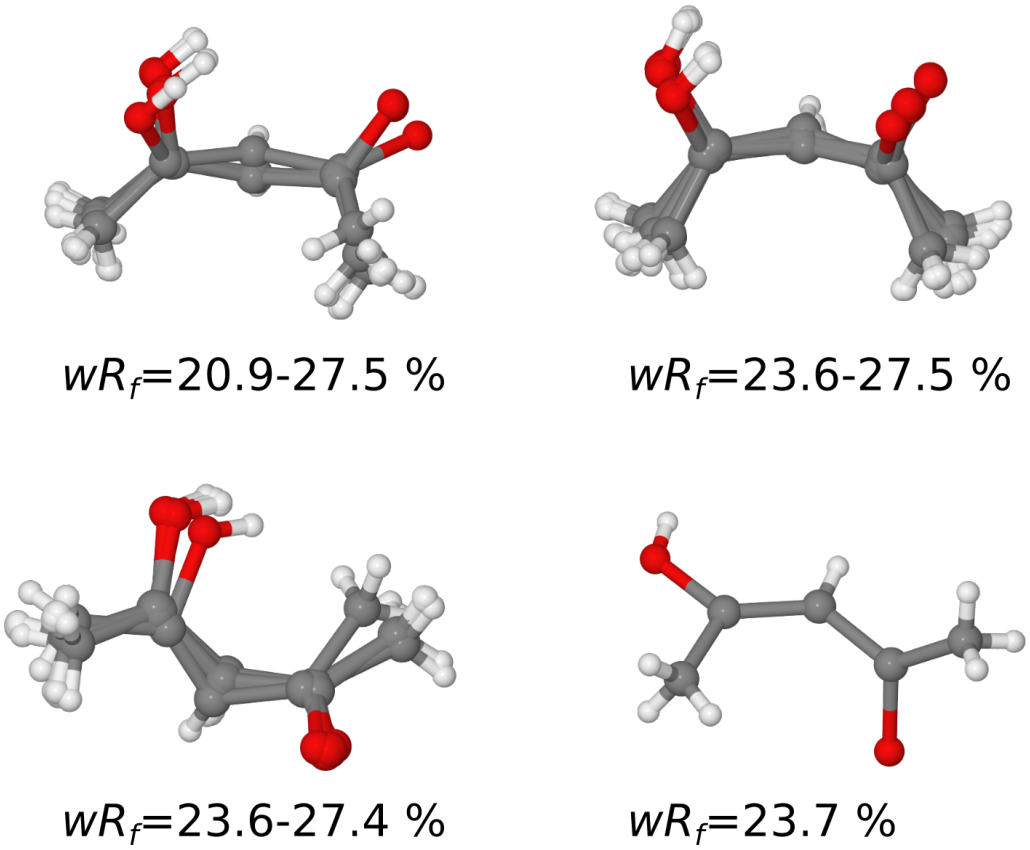

Figure 2.13: Comparison of the 25 AcAc structures refined from the analysis of intermediates' scattering curves ($sM^*(s)$). Clustering these structures resulted in four types of geometries.

(Fig. 2.14). The main reason for this increase is that the electronic excitation produces highly vibrationally excited molecules. The further internal conversion (IC), intersystem crossing (ISC), and intramolecular vibrational energy redistribution (IVR) produce vibrationally excited molecules. The high vibrational excitation appears as an increase of the vibrational amplitudes l, and the GED measures the averaged structures, where the $r_g = \langle r \rangle = r_e + \langle \delta r \rangle$, and the averaged displacement of the mean distance is connected to the vibrational amplitudes as[35]

$$\langle \delta r \rangle = -\frac{V_3}{2V_2} l^2 \ ,$$

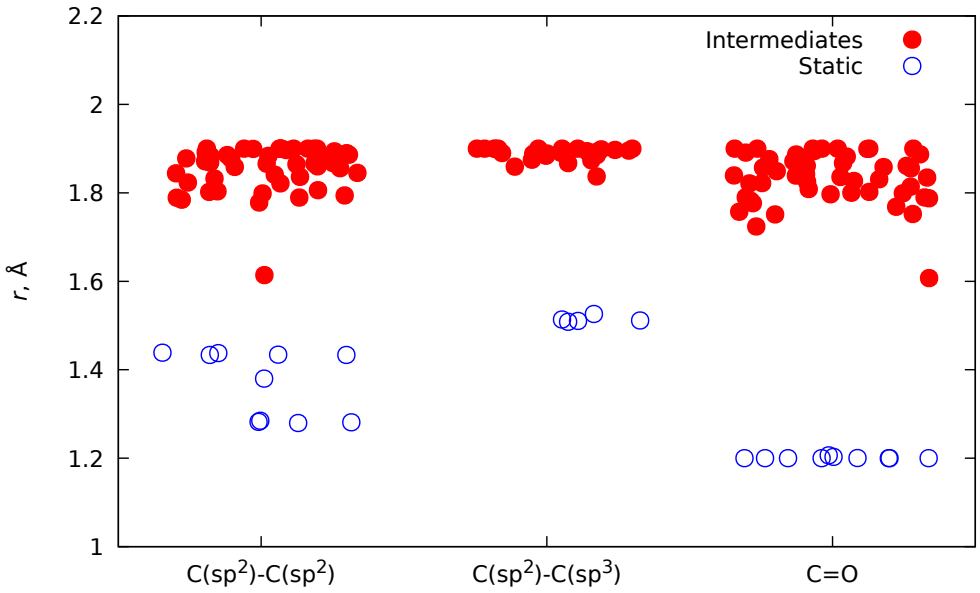

Figure 2.14: Comparison of the refined bond lengths for the static AcAc GED data and for the intermediates.

where V_2 and V_3 are the second and third derivatives of the potential energy surfaces versus bond distance. For the bonded distances, V_3 is usually negative, which means that with the increase of the vibrational amplitudes l the mean distances r_g tend to increase. The same increase can also be seen in $\Delta f_t(r)$ dependencies (Fig. 2.7).

2.4 Relaxation pathway at long delays

To explore the final relaxation stages of the system at the long pump-probe delays (above 2 ps), we additionally compared the experimental differential scattering curves with the theoretical ones computed at the B3LYP-D3(BJ)/def2-TZVPP level of theory. In the experimental conditions of one photon absorption the two possible final states are ro-vibrationally hot S_0 and long-lived T_1 states.[20, 42, 43] The photoexcited AcAc will thermalize via vibrational energy redistribution between the modes, and to simplify the analysis, we assume a fully thermalized theoretical model. The initial ensemble is assumed to be at the temperature of 323 K. To calculate the temperature of the final states, we optimized AcAc in the S_0 and T_1 states at the PBE0-D3(BJ)/def2-QZVPP level of theory, yielding the adiabatic energy difference between equilibrium geometries of these states to be 3.1 eV. The vertical excitation energy from the S_0 equilibrium structure to S_2 was found to be 5.2 eV, which is in discrepancy with the experimental excitation energy of 4.7 eV. Based on the theoretically derived energies, upon relaxation, the final hot S_0 state has 5.2 eV excess energy that is redistributed over 39 vibrational modes of AcAc yielding an excess temperature of 1541 K. This leads to a final temperature estimate for S_0 to be 1864 K. Similarly, the 2.1 eV of excess energy in T_1 leads to a final temperature estimate of 1233 K. The comparisons of the resulting theoretical difference $sM(s)$ and $f(r)$ curves are given in Figure 2.15.

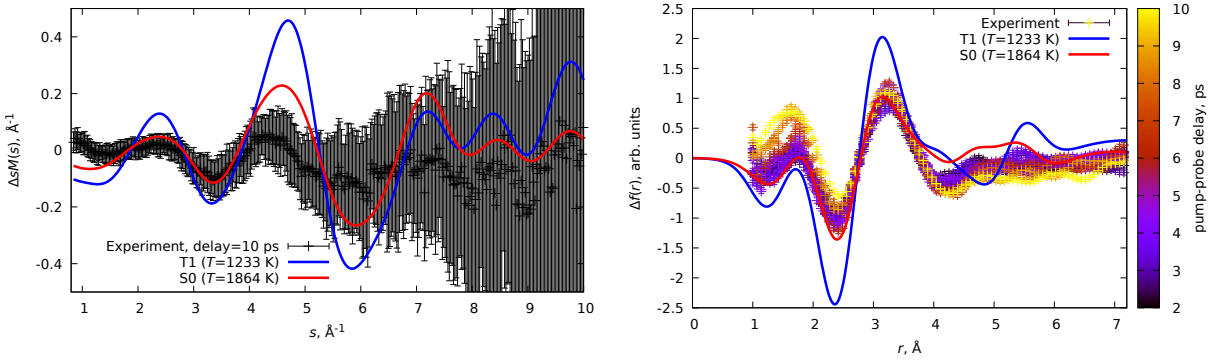

Figure 2.15: Left: Experimental 10 ps delay differential $sM(s)$ curve compared to theoretical analogs for the hot S_0 and hot T_1 states (left). The same data, but in the direct r-domain (right). Right: The theoretical scattering curves produced at the B3LYP-D3(BJ)/def2-TZVPP level of theory with respect to the initial state model of S_0 state with temperature of 323 K.

Both hot S_0 and T_1 show similar behavior, however, S_0 seems to fit better with the experimental observations.

Nevertheless, this cannot be a final assignment due to several assumptions, such as full thermalization and single state of the system.

2.5 UV power dependence

We investigated the dependence of the normalized differential UED signal on the UV pump laser power. To further reduce the impact of the slightly varying background level between scans, the integrated signal between 2.1-2.9 A^{-1} was subtracted from the integral of the 2.9-3.9 A^{-1} segment (Fig. 2.16). The signal grows linearly between 0.5 and 5 μJ/pulse that is consistent with single-photon excitation of AcAc by the pump pulse.

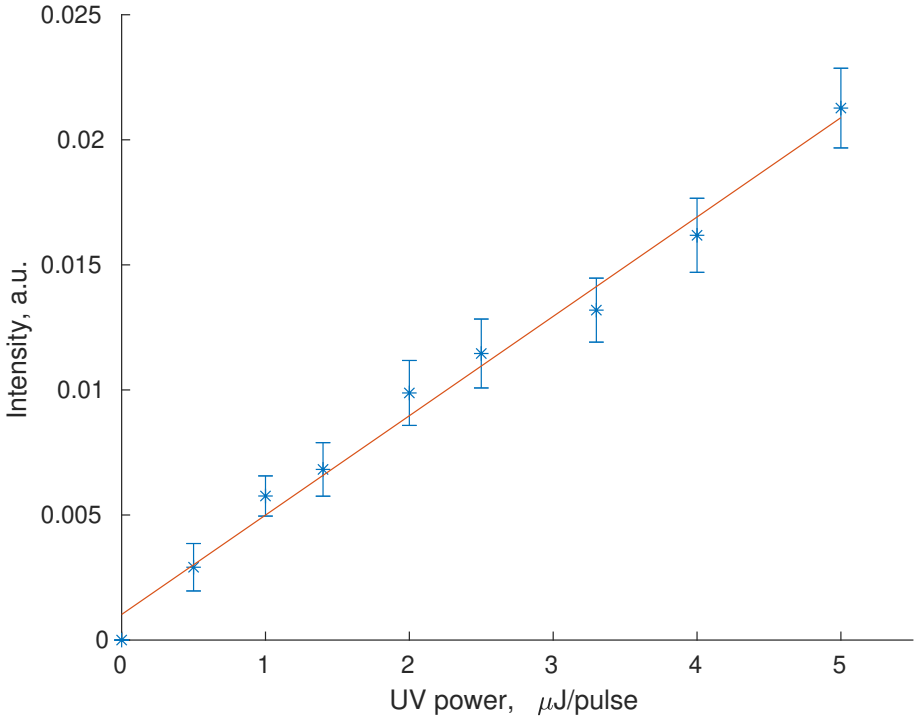

Figure 2.16: Pump power dependence of scattering signal (obtained by subtracting the integrated signal in the 2.1-2.9 A^{-1} segment from the 2.9-3.9 A^{-1} segment). The error bar represents one standard deviation of the set of measurements with applied bootstrapping.

Bibliography

[1] John C. Tully. Molecular dynamics with electronic transitions. *The Journal of Chemical Physics*, 93(2):1061–1071, 1990.

[2] Mario Barbatti. Nonadiabatic dynamics with trajectory surface hopping method. *WIREs Computational Molecular Science*, 1(4):620–633, 2011.

[3] Sebastian Mai, Martin Richter, Moritz Heindl, Maximilian F. S. J. Menger, Andrew Atkins, Matthias Ruckenbauer, Felix Plasser, Lea Maria Ibele, Simon Kropf, Markus Oppel, Philipp Marquetand, and Leticia González. Sharc2.1: Surface hopping including arbitrary couplings — program package for non-adiabatic dynamics. sharc-md.org, 2019.

[4] Martin Richter, Philipp Marquetand, Jesús González-Vázquez, Ignacio Sola, and Leticia González. SHARC: ab initio molecular dynamics with surface hopping in the adiabatic representation including arbitrary couplings. *J. Chem. Theory Comput.*, 7(5):1253–1258, 2011.

[5] Sebastian Mai, Philipp Marquetand, and Leticia González. Nonadiabatic dynamics: The sharc approach. *WIREs Comput. Mol. Sci.*, 8:e1370, 2018.

[6] Dermot Hegarty and Michael A. Robb. Application of unitary group methods to configuration interaction calculations. *Molecular Physics*, 38(6):1795–1812, 1979.

[7] Richard H.A. Eade and Michael A. Robb. Direct minimization in mc scf theory. the quasi-newton method. *Chemical Physics Letters*, 83(2):362–368, 1981.

[8] Jeppe Olsen. The casscf method: A perspective and commentary. *International Journal of Quantum Chemistry*, 111(13):3267–3272, 2011.

[9] J. Stephen Binkley, John A. Pople, and Warren J. Hehre. Self-consistent molecular orbital methods. 21. small split-valence basis sets for first-row elements. *Journal of the American Chemical Society*, 102(3):939–947, 1980.

[10] Mark S. Gordon, J. Stephen Binkley, John A. Pople, William J. Pietro, and Warren J. Hehre. Self-consistent molecular-orbital methods. 22. small split-valence basis sets for second-row elements. *Journal of the American Chemical Society*, 104(10):2797–2803, 1982.

[11] Ignacio Fdez. Galván, Morgane Vacher, Ali Alavi, Celestino Angeli, Francesco Aquilante, Jochen Autschbach, Jie J. Bao, Sergey I. Bokarev, Nikolay A. Bogdanov, Rebecca K. Carlson, Liviu F. Chibotaru, Joel Creutzberg, Nike Dattani, Mickaël G. Delcey, Sijia S. Dong, Andreas Dreuw, Leon Freitag, Luis Manuel Frutos, Laura Gagliardi, Frédéric Gendron, Angelo Giussani, Leticia González, Gilbert Grell, Meiyuan Guo, Chad E. Hoyer, Marcus Johansson, Sebastian Keller, Stefan Knecht, Goran Kovačević, Erik Källman, Giovanni Li Manni, Marcus Lundberg, Yingjin Ma, Sebastian Mai, João Pedro Malhado, Per Åke Malmqvist, Philipp Marquetand, Stefanie A. Mewes, Jesper Norell, Massimo Olivucci, Markus Oppel, Quan Manh Phung, Kristine Pierloot, Felix Plasser, Markus Reiher, Andrew M. Sand, Igor Schapiro, Prachi Sharma, Christopher J. Stein, Lasse Kragh Sørensen, Donald G. Truhlar, Mihkel Ugandi, Liviu Ungur, Alessio Valentini, Steven Vancoillie, Valera Veryazov, Oskar Weser, Tomasz A. Wesołowski, Per-Olof Widmark, Sebastian Wouters, Alexander Zech, J. Patrick Zobel, and Roland Lindh. Openmolcas: From source code to insight. *Journal of Chemical Theory and Computation*, 15(11):5925–5964, 2019. PMID: 31509407.

[12] Francesco Aquilante, Jochen Autschbach, Alberto Baiardi, Stefano Battaglia, Veniamin A. Borin, Liviu F. Chibotaru, Irene Conti, Luca De Vico, Mickaël Delcey, Ignacio Fdez. Galván, Nicolas Ferré, Leon Freitag, Marco Garavelli, Xuejun Gong, Stefan Knecht, Ernst D. Larsson, Roland Lindh, Marcus Lundberg, Per Åke Malmqvist, Artur Nenov, Jesper Norell, Michael Odelius, Massimo Olivucci, Thomas B. Pedersen, Laura Pedraza-González, Quan M. Phung, Kristine Pierloot, Markus Reiher, Igor Schapiro, Javier Segarra-Martí, Francesco Segatta, Luis Seijo, Saumik Sen, Dumitru-Claudiu Sergentu, Christopher J. Stein, Liviu Ungur, Morgane Vacher, Alessio Valentini, and Valera Veryazov. Modern quantum chemistry with [open]molcas. *The Journal of Chemical Physics*, 152(21):214117, 2020.

[13] A. D. Becke. Density-functional exchange-energy approximation with correct asymptotic behavior. *Phys. Rev. A*, 38:3098–3100, Sep 1988.

[14] Chengteh Lee, Weitao Yang, and Robert G. Parr. Development of the colle-salvetti correlation-energy formula into a functional of the electron density. *Phys. Rev. B*, 37:785–789, Jan 1988.

[15] Burkhard Miehlich, Andreas Savin, Hermann Stoll, and Heinzwerner Preuss. Results obtained with the correlation energy density functionals of becke and lee, yang and parr. *Chemical Physics Letters*, 157(3):200–206, 1989.

[16] Florian Weigend and Reinhart Ahlrichs. Balanced basis sets of split valence, triple zeta valence and quadruple zeta valence quality for h to rn: Design and assessment of accuracy. *Phys. Chem. Chem. Phys.*, 7:3297–3305, 2005.

[17] Frank Neese. The orca program system. *WIREs Computational Molecular Science*, 2(1):73–78, 2012.

[18] Frank Neese, Frank Wennmohs, Ute Becker, and Christoph Riplinger. The orca quantum chemistry program package. *The Journal of Chemical Physics*, 152(22):224108, 2020.

[19] Jmol development team. Jmol: an open-source java viewer for chemical structures in 3d. `http://www.jmol.org/`.

[20] R. J. Squibb, M. Sapunar, A. Ponzi, R. Richter, A. Kivimäki, O. Plekan, P. Finetti, N. Sisourat, V. Zhaunerchyk, T. Marchenko, L. Journel, R. Guillemin, R. Cucini, M. Coreno, C. Grazioli, M. Di Fraia, C. Callegari, K. C. Prince, P. Decleva, M. Simon, J. H. D. Eland, N. Došlić, R. Feifel, and M. N. Piancastelli. Acetylacetone photodynamics at a seeded free-electron laser. *Nature Communications*, 9(1):63, Jan 2018.

[21] István Hargittai. A survey: The gas-phase electron diffraction technique of molecular structure determination. In István Hargittai and Magdolna Hargittai, editors, *Stereochemical Applications of Gas Phase Electron Diffraction, Part A: The Electron Diffraction Technique*. VCH Publishers, Inc., New York, 1988.

[22] Takeshi Yanai, David P Tew, and Nicholas C Handy. A new hybrid exchange–correlation functional using the coulomb-attenuating method (cam-b3lyp). *Chemical Physics Letters*, 393(1):51–57, 2004.

[23] Yury V. Vishnevskiy. UNEX version 1.6, `http://unexprog.org` (accessed Tue May 03, 2022).

[24] A. W. Ross, M. Fink, R. Hilderbrandt, J. Wang, and V. H. Jr Smith. Complex scattering factors for the diffraction of electrons by gases. In E. Prince, editor, *International Tables for Crystallography Volume C: Mathematical, physical and chemical tables*, pages 262–391. Kluwer Academic Publishers, Dordrecht/Boston/London, third edition edition, 2004.

[25] M. Lentzen. Relativistic correction of atomic scattering factors for high-energy electron diffraction. *Acta Cryst. A*, 75(6):861–865, 2019.

[26] Denis S. Tikhonov. Regularized weighted sine least-squares spectral analysis for gas electron diffraction data. *The Journal of Chemical Physics*, 159(17):174101, 11 2023.

[27] Yury V. Vishnevskiy, Maxim A. Abaev, Anatolii N. Rykov, Mikhail E. Gurskii, Pavel A. Belyakov, Sergey Yu. Erdyakov, Yuri N. Bubnov, and Norbert W. Mitzel. Structure and bonding nature of the strained lewis acid 3-methyl-1-boraadamantane: A case study employing a new data-analysis procedure in gas electron diffraction. *Chemistry – A European Journal*, 18(34):10585–10594, 2012.

[28] Denis S. Tikhonov, Yury V. Vishnevskiy, Anatolii N. Rykov, Olga E. Grikina, and Leonid S. Khaikin. Semi-experimental equilibrium structure of pyrazinamide from gas-phase electron diffraction. how much experimental is it? *Journal of Molecular Structure*, 1132:20–27, 2017. Gas electron diffraction and molecular structure.

[29] Natalya V. Belova, Heinz Oberhammer, Nguen Hoang Trang, and Georgiy V. Girichev. Tautomeric properties and gas-phase structure of acetylacetone. *The Journal of Organic Chemistry*, 79(12):5412–5419, 2014. PMID: 24758690.

[30] Carlo Adamo and Vincenzo Barone. Toward reliable density functional methods without adjustable parameters: The pbe0 model. *The Journal of Chemical Physics*, 110(13):6158–6170, 1999.

[31] Stefan Grimme, Stephan Ehrlich, and Lars Goerigk. Effect of the damping function in dispersion corrected density functional theory. *Journal of Computational Chemistry*, 32(7):1456–1465, 2011.

[32] Yury V Vishnevskiy and Yuriy A Zhabanov. New implementation of the first-order perturbation theory for calculation of interatomic vibrational amplitudes and corrections in gas electron diffraction. *Journal of Physics: Conference Series*, 633:012076, sep 2015.

[33] Axel D. Becke. Density-functional thermochemistry. iii. the role of exact exchange. *The Journal of Chemical Physics*, 98(7):5648–5652, 1993.

[34] Otto Bastiansen, Kari Kveseth, and Harald Møllendal. Structure of molecules with large amplitude motion as determined from electron-diffraction studies in the gas phase. In *Large Amplitude Motion in Molecules I*, pages 99–172, Berlin, Heidelberg, 1979. Springer Berlin Heidelberg.

[35] Yury V. Vishnevskiy and Denis Tikhonov. Quantum corrections to parameters of interatomic distance distributions in molecular dynamics simulations. *Theoretical Chemistry Accounts*, 135(4):88, Mar 2016.

[36] Denis S. Tikhonov, Dmitry I. Sharapa, Jan Schwabedissen, and Vladimir V. Rybkin. Application of classical simulations for the computation of vibrational properties of free molecules. *Phys. Chem. Chem. Phys.*, 18:28325–28338, 2016.

[37] Thomas E. Markland and Michele Ceriotti. Nuclear quantum effects enter the mainstream. *Nature Reviews Chemistry*, 2(3):0109, Feb 2018.

[38] Rainer Storn and Kenneth Price. Differential evolution – a simple and efficient heuristic for global optimization over continuous spaces. *Journal of Global Optimization*, 11(4):341–359, Dec 1997.

[39] Pauli Virtanen, Ralf Gommers, Travis E. Oliphant, Matt Haberland, Tyler Reddy, David Cournapeau, Evgeni Burovski, Pearu Peterson, Warren Weckesser, Jonathan Bright, Stéfan J. van der Walt, Matthew Brett, Joshua Wilson, K. Jarrod Millman, Nikolay Mayorov, Andrew R. J. Nelson, Eric Jones, Robert Kern, Eric Larson, C J Carey, İlhan Polat, Yu Feng, Eric W. Moore, Jake VanderPlas, Denis Laxalde, Josef Perktold, Robert Cimrman, Ian Henriksen, E. A. Quintero, Charles R. Harris, Anne M. Archibald, Antônio H. Ribeiro, Fabian Pedregosa, Paul van Mulbregt, and SciPy 1.0 Contributors. SciPy 1.0: Fundamental Algorithms for Scientific Computing in Python. *Nature Methods*, 17:261–272, 2020.

[40] I.V. Kochikov, Yu.I. Tarasov, G.M. Kuramshina, V.P. Spiridonov, A.G. Yagola, and T.G. Strand. Regularizing algorithm for determination of equilibrium geometry and harmonic force field of free molecules from joint use of electron diffraction, vibrational spectroscopy and ab initio data with application to benzene. *Journal of Molecular Structure*, 445(1):243–258, 1998. Gas Electron Diffraction: Molecular Structure and Conformational Analysis.

[41] Denis S. Tikhonov. `https://stash.desy.de/projects/MOLINC`, 2020.

[42] Aditi Bhattacherjee, Chaitanya Das Pemmaraju, Kirsten Schnorr, Andrew R. Attar, and Stephen R. Leone. Ultrafast intersystem crossing in acetylacetone via femtosecond x-ray transient absorption at the carbon k-edge. *Journal of the American Chemical Society*, 139(46):16576–16583, 2017. PMID: 29083165.

[43] Marin Sapunar, Tarek Ayari, and Nada Došlić. Comparative study of the photodynamics of malonaldehyde and acetylacetone. *Chemical Physics*, 515:622–627, 2018.